



Post plasma-catalysis for total oxidation of trichloroethylene over Ce–Mn based oxides synthesized by a modified “redox-precipitation route”

M.T.Nguyen Dinh^{a,1}, J.-M. Giraudon^{a,*}, A.M. Vandenbroucke^b, R. Morent^b, N. De Geyter^b, J.-F. Lamonier^a

^a Université Lille1, Sciences et Technologies, Unité de Catalyse et Chimie du Solide UMR CNRS UCCS 8181, 59655 Villeneuve d'Ascq, France

^b Ghent University, Faculty of Engineering and Architecture, Department of Applied Physics, Research Unit Plasma Technology, Sint-Pietersnieuwstraat 41, 9000 Ghent, Belgium

ARTICLE INFO

Article history:

Received 4 December 2014

Received in revised form 29 January 2015

Accepted 10 February 2015

Available online 12 February 2015

Keywords:

Non- thermal plasma
Plasma-catalysis
Trichloroethylene
Ozone
Cerium
Manganese
Chlorinated-VOCs removal

ABSTRACT

Two CeMn_xO_y (CeMn_x) catalysts ($x = 1$, CeMn ; $x = 4$; CeMn_4) were synthesized via a modified “redox-precipitation” route followed by calcination at 500°C . XRD analysis showed only the presence of ceria. Raman spectroscopy gave a featureless spectrum for CeMn while peaks characteristic of a birnessite-type structure were observed for CeMn_4 oxide. A large surface area of $165 \text{ m}^2/\text{g}$ was obtained for CeMn which decreased to $95 \text{ m}^2/\text{g}$ with $x = 4$. Furthermore XPS characterizations showed homogeneous distribution of the active phase. Trichloroethylene (TCE) abatement was investigated at 150°C with catalyst alone, non-thermal plasma (NTP) alone at ambient conditions and with a post plasma-catalytic (PPC) system using these cerium–manganese oxides as well as a reference Mn oxide as catalysts positioned downstream of the plasma. At 150°C , without NTP, MnO_2 converted specifically 5% of TCE into CO_2 while volatile organic compound (VOC) adsorption mainly occurred over the other catalysts. With NTP alone, 87% TCE removal was achieved at 240 J/L but formation of unwanted polychlorinated by-products, such as phosgene, dichloroacetylchloride and trichloroacetaldehyde occurred resulting in a low CO_x ($x = 1, 2$) selectivity of about 27%. In comparison, a significant improvement was observed in TCE abatement performance when using the PPC configuration. Indeed, TCE conversion up to about 100% as well as CO_x selectivity up to 56% were achieved thanks to the high efficiency of the catalysts to completely decompose O_3 leading to the production of active oxygen species which are able to oxidize the by-products. The best plasma-assisted catalyst performance observed for CeMn_4 may be linked to the presence of residual potassium allowing to avoid the poisoning of catalytic sites with chlorinated organic species as well as slowing down the formation of chlorinated mineral phases.

© 2015 Published by Elsevier B.V.

1. Introduction

Development and optimization of different processes for volatile organic compounds (VOCs) treatment, mainly originating from gaseous industrial effluents, are crucial issues for the improvement of air quality. Due to increasingly restrictive legislations more stringent value limits regarding VOC concentrations have to be implemented. As a result, the treatment of this low concentrated air

pollution seems less attractive by means of conventional physico-chemical treatments (thermal or catalytic oxidation, absorption or adsorption). However, the combination of various techniques may be crucial to overcome these technological drawbacks. Among those, the combination of non thermal plasma (NTP) and heterogeneous oxidation catalysis has been recently considered as one of these emerging technologies [1–5]. NTP assisted catalysis is able to eliminate toxic pollutants at low temperature due to a higher energy efficiency leading to a low energy cost. Furthermore, the development of a suitable catalyst will help to optimize the selectivity into environmentally more friendly end products. The plasma reactor can be coupled with the catalyst in two different configurations depending on the catalyst location respective to the

* Corresponding author. Tel.: +33 320436856.

E-mail address: jean-marc.giraudon@univ-lille1.fr (J.-M. Giraudon).

¹ Present address: The University of Da-Nang, University of Science and Technology, 54, Nguyen Luong Bang, Da-Nang, Vietnam.



position of the plasma reactor: by introducing the catalyst in the discharge zone (in plasma-catalysis, IPC) [6–12] or by placing the catalyst downstream of the discharge zone (post plasma-catalysis, PPC) [13–16]. Whatever the configuration under concern, adding a catalyst enhances the energy efficiency, carbon mass–balance and mineralization degree of the VOC compared to NTP systems alone. One major drawback of using NTP in a VOC/air mixture is that plasma generated oxygen radicals can quickly react with molecular oxygen to produce ozone. This secondary pollutant is well known to be a respiratory hazard having adverse effects on humans. The PPC process, for its part, takes advantages of the NTP emitted O₃ as a potential source of very active oxygen species able to greatly improve the oxidation of both the target VOC and potential gaseous hazardous by-products. This advantage is directly related to the catalyst efficiency regarding the ozone decomposition.

Among the transition-metal catalysts, high valence manganese oxides are well recognized as active O₃ decomposition catalysts [17,18]. As surface area can play an important role in O₃ decomposition, dispersion of MnO_x is thought to be greatly improved by forming Mn–Ce binary oxides, CeO₂ being also known to decompose ozone [18]. With that respect, new CeMn_xO_y oxides have been previously synthesized by the “driving redox-precipitation reactions synthesis” developed by Arena et al. [19–21]. It has been reported that these new nanostructured CeMn_xO_y catalysts possess superior textural and redox properties in comparison to co-precipitated systems. Indeed, the resulting strong MnO_y–CeO₂ interaction along with higher average oxidation number of both Mn and Ce ions have been claimed to be responsible for the strong promotion of the reactive surface oxygen availability and the CO oxidation activity in the range of 50–150 °C [21].

In general, chlorinated air pollutants are difficult to remediate as they are relatively stable. Therefore, trichloroethylene (TCE) is used here as a VOC model compound. This chlorinated VOC is a commonly used industrial solvent and acts as a degreaser in the semiconductor and metal industry. According to the International Agency for Research on Cancer (IARC), TCE belongs to the group 2A which means it is probably carcinogenic to humans. However, TCE is easily removed by NTP without the addition of considerable energy. This results from the fact that reactive radicals, produced in the plasma discharge, easily add to the carbon–carbon double bond thereby initiating the oxidation process. However, the application of NTP for chlorinated VOC remediation is impeded by low energy efficiency and low CO₂ selectivity due to the formation of polychlorinated compounds which can be more toxic than the target VOC. Over the last decade some NTP reactors and catalysts combinations were tested for TCE abatement to overcome the drawbacks of the NTP technology [4]. In comparison to in-plasma catalysis processes post-plasma catalysis combinations are rather scarce. In our case we choose PPC technology and the adopted design of the NTP reactor is here a 5 pins to plate configuration using a DC negative corona discharge working in a stabilized luminescent glow regime characterized by an intense gas ionization in the whole discharge gap. This NTP reactor is cost-saving, easy to scale-up and allows to work at atmospheric and room temperature with high flow rates compared to in-plasma processes. Furthermore use of CeMn oxides in the combined system has not been reported so far in PPC experiments despite of their high performances in TCE total oxidation.

In this work, TCE abatement was investigated in moist air (RH = 10%) containing a small amount of CO₂ (520 ppmv) at 150 °C with catalyst alone, NTP alone at ambient conditions and with a PPC system. The studied catalysts were two dispersed CeMn_x oxide catalysts ($x = 1, 4$) prepared by a modified procedure inspired from the “redox-precipitation” route previously described and one reference MnO_y catalyst. The catalytic reactor was placed downstream of a DC-excited negative corona multi-pin-to- plate discharge reactor.

Particular attention has been paid to investigate the performance of the plasma-assisted catalysts for TCE abatement and to make a correlation with the physico-chemical properties of the tested catalysts.

2. Experimental

2.1. Catalysts preparation

2.1.1. Synthesis of the CeMn_x catalysts

The KMnO₄ precursor was titrated with an aqueous solution of Ce³⁺ (Ce(NO₃)₃·6H₂O (Alfa Aesar 99.5%) and Mn²⁺ ions (Mn (NO₃)₂·4H₂O, 99.98%, Aldrich) at varying pH (from 3.0 to 8.0) considering the redox reactions under concern [19]. The amount of the various precursors was determined in accordance with the quantitative relationships provided by the system of equations previously given in [19] referring to electron and mass balances and the designed catalyst composition, respectively [19]. In a typical experiment a suitable amount of KMnO₄ (Fluka, 99%), in excess of 10% from the stoichiometry, dissolved in 40 ml of deionized water was added to the metal nitrate precursors aqueous solution (30 ml). A KOH solution (0.2 M solution) was then added dropwise, under constant stirring, to a final pH of 8.0 (±0.5). The solid was then digested for 30 min, subsequently filtered, washed with distilled water several times and dried overnight at 100 °C. The resulting powders were further calcined in air at 500 °C (4 h). The Ce–Mn based samples were labeled CeMn_x ($x = 1, 4$).

2.1.2. Synthesis of the MnO_y catalyst

Ammonia (Verbièse, 25%) was added dropwise to an aqueous solution of the Mn nitrate precursor (Mn (NO₃)₂·4H₂O, 99.98%, Aldrich) under constant stirring until the pH reached a value of 10.0. The resulting solid was then kept under stirring for 15 min. After filtration and washing, the solid was dried overnight at 100 °C and subsequently calcined in a similar procedure as above to yield the MnO_y catalyst.

2.2. Catalysts characterization

Phase analysis was performed by X-ray powder diffraction using a D8 Advance-Brücker using the $K_{Cu\alpha 1} = 1.5406 \text{ \AA}$. The data of 2θ in the 10–90° were collected with a step size of 0.02° and an integration time of 5 s. The diffraction patterns were indexed by comparison with the Joint Committee on Powder Diffraction Standards (JCPDS) files.

The specific surface areas were measured with Tristar II 3020 (Micromeritics) set-up. Prior to measurement, the catalysts were pre-heated at 150 °C in flowing N₂ for 1 h.

The Laser Raman Spectra (LRS) of the samples were recorded on a LabRam Infinity (Jobin Yvon – Horiba) spectrometer equipped with a liquid nitrogen cooled CCD detector and a frequency-doubled Nd:YAG green laser at 532 nm. The power applied on the sample was 60 μW for the Ce–Mn samples as higher applied power led to phase transformation leading to CeO₂ and Mn₃O₄ due to sample-heating phenomenon [19].

XPS spectra of the samples were recorded using a Kratos AXIS Ultra DLD spectrometer with a monochromatic Al K α radiation source ($h\nu = 1486.7 \text{ eV}$) operating at 15 kV and 10 mA. High resolution (0.1 eV) spectra were then recorded for pertinent photo-electron peaks at pass energy of 40 eV to identify the chemical state of each element. All the binding energies (BEs) were referenced to the C1s neutral carbon peak at 285 eV. The processing and curve-fitting of the high resolution spectra were performed using CasaXPS™ software.

2.3. Experimental set-up

The scheme of the experimental set-up was already given in reference [22]. It consisted of a reaction gas supply system, a 5-pin-to-plate plasma source (30 kV/20 mA) negative DC power supply), a post plasma catalytic reactor and analytical instrumentation. Total oxidation of TCE was carried out in air supplied by a compressor (RH:10%; CO₂:520 ppmv). Gaseous TCE-contaminated air was produced by passing air through pure liquid TCE kept in a water bath at fixed temperature. Further dilution in air was achieved in order to get a TCE concentration in the range of 360–400 ppmv. The total gas flow rate in all experiments was 120 L/h. The multi-pin-to-plate plasma source was based on the concept of a negative DC glow discharge [23,24]. A detailed description of the geometry of the plasma reactor and electrical measurements were published elsewhere [25]. The electron density and energy of the discharge were approximately 10⁸–10⁹ electrons cm⁻³ and 2–3 eV, respectively [26]. The production of ozone by this source was described in [27]. The catalytic reactor was cylindrical and connected to the NTP reactor in series. This reactor was made in Pyrex glass, with an inner diameter of 2.0 cm and an effective length of 10.0 cm.

2.4. Experimental procedure

The catalyst (1 g) was submitted to a flow of TCE (360–400 ppm) diluted in humid air (RH: 10%; CO₂: 520 ppmv) for 2–3 h at ambient conditions and was then heated to 150 °C and kept at this temperature for 1 h. At this stage, the plasma was turned on and the energy density was changed every 30 min. The TCE abatement and the identification of the gaseous by-products were carried out with a FT-IR spectrometer (Bruker, Vertex 70). The optical length of the gas cell and the resolution of the spectrometer were set at 20 cm and 4 cm⁻¹, respectively. The formation of ozone was analyzed by an UV ozone monitor (Envitec, model 450).

The following parameters were used to evaluate the process efficiency:

$$\text{TCE removal efficiency} : \eta_{\text{TCE}}(\%) = \left(\frac{1 - [\text{TCE}]_{\text{out}}}{[\text{TCE}]_{\text{in}}} \right) \times 100 \quad (1)$$

where [TCE]_{in} is the concentration introduced in the reactor and [TCE]_{out} is the concentration at the exit of the catalytic reactor.

The CO, CO₂ and CO_x selectivities are defined as:

$$S_{\text{CO}}(\%) = \frac{[\text{CO}]}{(2 \times [\text{TCE}]_{\text{conv}})} \times 100 \quad (2)$$

$$S_{\text{CO}_2}(\%) = \frac{[\text{CO}_2]}{(2 \times [\text{TCE}]_{\text{conv}})} \times 100 \quad (3)$$

where [CO] and [CO₂] are the concentration of CO and CO₂ corrected from the atmospheric CO₂ at the exit of the reactor, respectively.

$$S_{\text{CO}_x}(\%) = S_{\text{CO}} + S_{\text{CO}_2} \quad (4)$$

Y_{CO} and Y_{CO₂} are the yields of CO and CO₂, respectively, that are defined as:

$$Y_{\text{CO}}(\%) = \frac{[\text{CO}]}{2 \times [\text{TCE}]_{\text{in}}} \times 100 \quad (5)$$

$$Y_{\text{CO}_2}(\%) = \frac{[\text{CO}_2]}{2 \times [\text{TCE}]_{\text{in}}} \times 100 \quad (6)$$

$$\text{Energy Density} : \text{ED} \left(\frac{J}{L} \right) = \frac{W(J/s)}{Q(L/s)} \quad (7)$$

where W is the discharge power and Q is the flow rate.

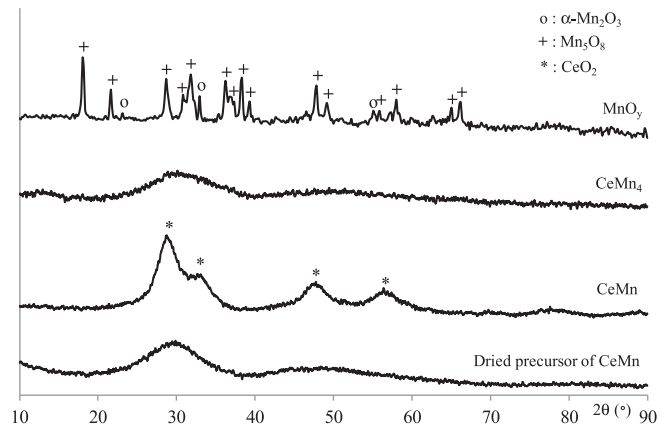


Fig. 1. XRD patterns of the fresh catalysts.

3. Results

3.1. Catalysts properties

The diffractograms of the dried samples consist of a broad 2θ component (20–40°) followed by a large envelop (40–70°) indicative of solid architecture missing substantial “long-range” crystalline order. The diffractogram of the calcined CeMn oxide displayed in Fig. 1 exhibits the characteristic peaks of the CeO₂ fluorite-like phase (JCPDS 00-004-0593) with no shift in 2θ of the peak position with Mn content. The XRD pattern of the calcined CeMn₄ is rather similar to that of the dried precursor of CeMn sample and compared well with diffractograms recorded for extremely dispersed ceria systems [28–30]. The XRD pattern of MnO_y shows peaks of higher intensity ascribed to the monoclinic phase of the metastable Mn₅O₈ (Mn₃⁴⁺, Mn₂²⁺) (JCPDS 00-039-1218) phase along with other peaks of lower intensity ascribed to the cubic phase α- Mn₂O₃ (Mn₂³⁺, Mn²⁺) (JCPDS 01- 089-2809). From the height ratio of the most intense peaks of each phase (2θ=18° – Mn₅O₈; 2θ=32.9° – α-Mn₂O₃) a rough estimation of the Mn₅O₈ percentage in the powder mixture gives a value of 70%. The S_{BET} values are characterized by a large surface exposure in the calcined CeMn sample (165 m²/g) which decreases to 95 m²/g when the Mn loading increases (CeMn₄). It is noticeable that the CeMn sample develops an outstanding surface exposure of 165 m²/g close to the one of 154 m²/g reported by Arena et al. but obtained at a calcination temperature 100 °C lower than ours [19]. Contrarily, the specific surface area of the MnO_y sample is only 13 m²/g. Regarding the XPS results, the Mn/(Ce + Mn)_{XPS} atomic ratio in function of the nominal value Mn/(Ce + Mn) affords a straight-line with a slope value of 1.0 indicating a (quasi) molecular dispersion of the active phase in the different samples. The enhanced textural properties developed by the samples along with the absence of substantial “long-range” crystalline order as well as the similarity in terms of surface and bulk composition accounts for the beneficial effect of the synthesis route compared to the co-precipitation synthesis in accordance with the works of Arena et al. [19]. The average oxidation state (AOS) of manganese was determined by XPS from the relation based on a correlation between the binding energies of the doublet separation of Mn3s (ΔE_{s}) and the AOS, AOS = 8.956 – 1.13 ΔE_{s} , given by Galakhov et al. [31]. An AOS value higher than 3.0 is found: 3.3 and 3.5, for the CeMn and CeMn₄ samples, respectively.

Because of its sensitivity to amorphous components and those with short-range order, Raman spectroscopy is very useful to study the structure of MnO_y materials where crystalline disorder may be expected. The LRS of the CeMn sample (Fig. 2) shows a mostly amorphous pattern in line with the lack of any long range crystalline order consistent with the results of Arena et al. [21].

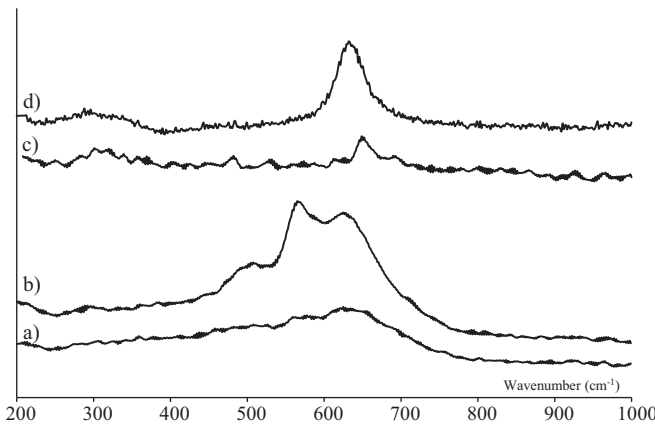


Fig. 2. LRS of the fresh samples: (a) CeMn; (b) CeMn₄; (c) and (d) MnO_y.

All the LRS of CeMn₄ show similar features of birnessite-type MnO₂ with layered structure having a low Raman activity [32,33]. Three major peaks can be evidenced at 510, 565 and 625 cm⁻¹ with the two high wavenumber peaks dominating all spectra. Indeed, three major features have been previously reported at 500–510, 575–585 and 625–650 cm⁻¹ regarding such materials [34]. It is noticeable that the frequency position of these major Raman-active modes can change as a function of the average MnO₆ octahedral polymerization in several manganese oxide structures [35]. This result substantiates the XRD observation of the presence of a possible birnessite phase having a large diffraction peak at $2\theta = 12^\circ$ (Fig. 1). Regarding the LRS of the MnO_y sample an LRS with high Raman

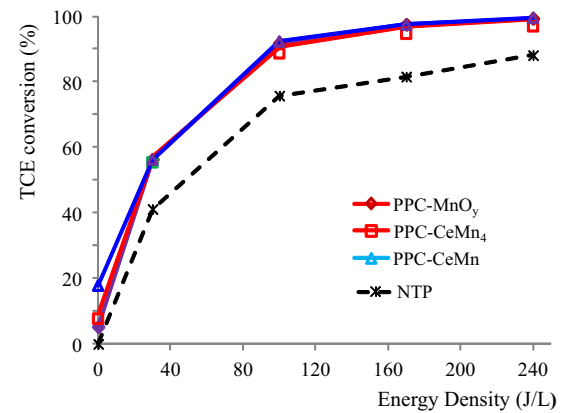


Fig. 3. TCE conversion in function of the energy density.

activity having the features characteristic of α - Mn₂O₃ (Fig. 2c) [36] with a large peak positioned at 634 cm⁻¹ is found. Other spectra show a low Raman activity displaying weak peaks at 480, 535, 620 cm⁻¹ as well as a more intense one positioned at 649 cm⁻¹ characteristic of the metastable Mn₅O₈ oxide species (Fig. 2d) [37].

3.2. TCE decomposition efficiency

Fig. 3 shows the evolution of η_{TCE} in function of the energy density relative to NTP in NTP (room temperature) and PPC experiments (NTP: room temperature; catalytic reactor: 150 °C). Regarding the NTP experiment, the TCE abatement increases with ED due to the formation of more energetic electrons to reach a

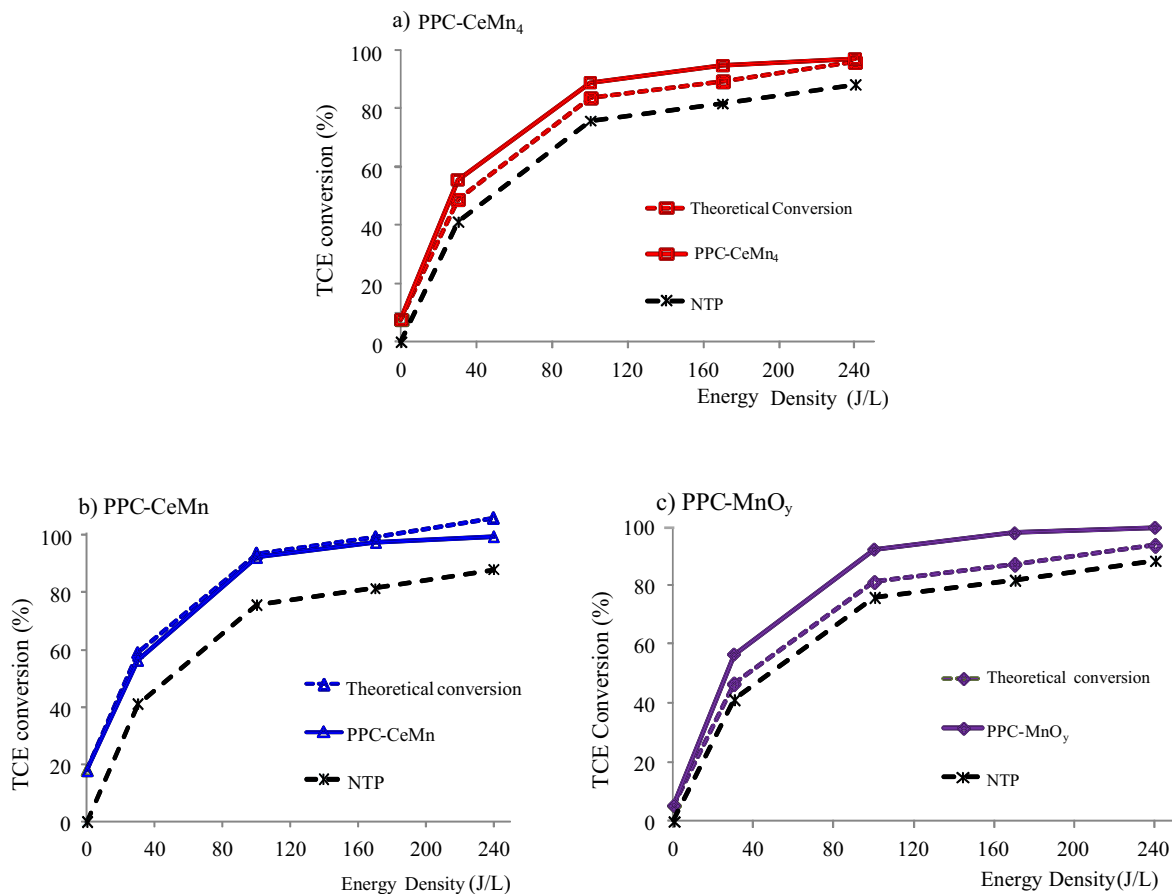


Fig. 4. Representation of $(\eta_{TCE})_{NTP}$, $(\eta_{TCE})_{cat}$ and $(\eta_{TCE})_{NTP} + (\eta_{TCE})_{cat}$ in function of the energy density.

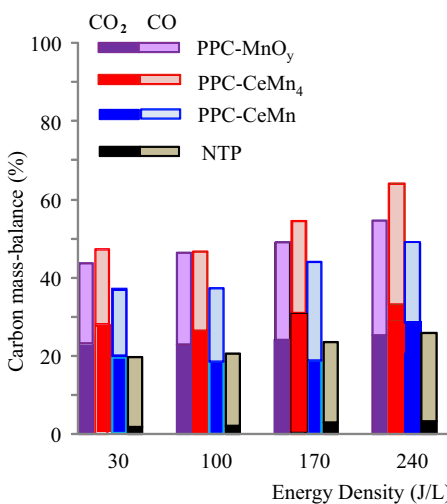


Fig. 5. Mass carbon balance for the PPC process in function of the ED.

TCE removal efficiency of 87% at 240 J/L. However, the CO_x selectivity is still low spanning from 20 to 27% whatever ED used. Furthermore, the gas discharge also induces the formation of ozone as hazardous by-product whose production increases with ED to 350 ppm at 240 J/L. The reactivity for TCE degradation has been then investigated over the catalysts without NTP at 150 °C after a pre-calcination step at 350 °C. The samples can be ranked by increasing TCE conversion (η_{TCE})_{cat} as follows: MnO_y (5%) < CeMn₄ (8%) < CeMn (18%). Based on the formula of TCE conversion used herein, although CO₂ is the only detected gaseous compound, TCE adsorption on the catalyst may also account for such values. Thus, from carbon-mass balance (CMB) results, it is found that the MnO_y catalyst is highly selective into CO₂ having a CMB close to 100%. However, the low CMBs of 40 and 17% observed for CeMn₄ and CeMn samples, respectively, can mainly be attributed to TCE adsorption in accordance with their porous nature. Also, as expected, the high weight hourly space velocity (WHSV) of 120 L h⁻¹ g⁻¹ precludes having high TCE conversion on these catalysts without NTP.

The evolution of η_{TCE} in function of energy density in PPC experiments (Figs. 3 and 4) displays a similar behavior to the one observed for NTP alone but are translated to higher η values for a given ED. However it has to be stressed that a direct comparison is not possible in terms of an energetic point of view as the extra input energy to maintain the catalytic reactor to 150 °C has not been considered. At 240 J/L, high TCE conversion can be achieved following the increasing sequence: CeMn₄ (96.9%) < MnO_y (99.3%) ≈ CeMn (99.5%). Fig. 4 also shows that, for a given ED, the η_{TCE} achieved with plasma-catalysis is higher than the theoretical TCE conversion (η_{TCE})_{th} which is the summation of those of plasma-alone (η_{TCE})_{NTP} and catalyst-alone (η_{TCE})_{cat} whatever ED used for MnO_y oxide and up to 170 J/L for the CeMn₄ sample. On the other hand, it is found that the experimental and theoretical curves superimpose up to 170 J/L for CeMn sample. However, as the TCE consumption with the catalyst alone is mostly related to adsorption for CeMn, the theoretical curve is overestimated. As a result, the experimental curve should also have been higher than the true theoretical curve. Hence, it is observed a synergistic effect by combining both NTP and MnO_y catalyst or in interaction with CeO_x. This effect can be related to the efficiency of MnO_y and CeO₂ to dissociatively decompose ozone. This reaction enables the supply of additional active oxygen species that assist the destruction of remaining TCE exiting the plasma reactor. Indeed, MnO₂ is well recognized to be the best bulk catalyst for this reaction [18].

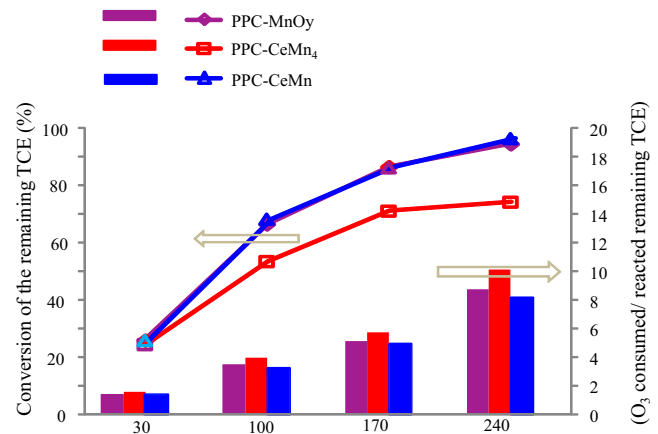


Fig. 6. TCE conversion and molar ratio $R_{(O_3/TCE)}$ (O₃ consumed/reacted remaining TCE) in function of ED.

Fig. 5 shows the CMB expressed in terms of CO_x selectivities in function of ED. For PPC experiments, a 1.5 to 2-fold increase of the CMB was observed whatever the ED used. For a η_{TCE} of about 95–100%, the CMB values reach 50–65% along with molar CO₂/CO_x ($x = 1, 2$) ratios of 0.45–0.60 compared to 26% and 0.15 with NTP, respectively. Hence, the rate of TCE mineralization increased with the hybrid process, promoting the CO₂ production at the expense of CO.

Fig. 6 displays the remaining TCE conversion $\eta_{TCE\text{-remaining}}$, which is the rate of destruction of the NTP unreacted TCE over the catalysts under study as well as the molar ratio $R_{(O_3/TCE)}$ (O₃ consumed/reacted remaining TCE) in function of the ED. Ease of destruction of the NTP unreacted TCE increases over the assisted catalysts irrespective of the ED as follows: CeMn₄ < MnO_y ≈ CeMn. Regarding the plasma-assisted MnO_y and CeMn samples having the same specific activity, it is found that the intrinsic activity on MnO_y r_{TCE} (MnO_y) is about 13 times higher than the intrinsic activity on CeMn r_{TCE} (CeMn) taking into account the ratio of the specific surface area of the catalysts. Although the Mn content for the CeMn sample is twice as small as that of the MnO_y sample, the value of the relative ratio of the intrinsic rates shows that the quality (nature) of the active sites has to be considered. The reaction with O₃ is in line with the formal equation:



It is noticeable that the $R_{(O_3/TCE)}$ values become higher than 4 for ED higher than 170 J/L for both catalysts. This can be attributed to the greater ability of all the catalysts to oxidize the NTP gaseous polychlorinated intermediates using O₃. The higher $R_{(O_3/TCE)}$ for CeMn₄ irrespective of ED reflects the better reactivity of this catalyst to transform such gaseous by-products at the expense of the NTP non processed TCE. Fig. 7 sums up the performance in terms of TCE conversion, CO₂ and CO_x yields of the different processes: total catalytic oxidation, NTP and PPC. Whatever the parameter under concern, PPC was found to be the best alternative to convert TCE into CO₂ while CeMn₄ was found to be the best NTP assisted catalyst in terms of CO₂ selectivity.

3.3. Detection of the gaseous by-products by FT-IR

Figs. 8 and 9 show the FT-IR spectra of both the inlet and outlet streams when the plasma reactor is operated at 240 J/L with or without catalysts. By carefully comparing these figures with the NIST IR spectra standard reference database, the TCE abatement in NTP is supported by a strong decrease of the absorption bands at 935–945 cm⁻¹. FT-IR reveals formation of phosgene (PG),

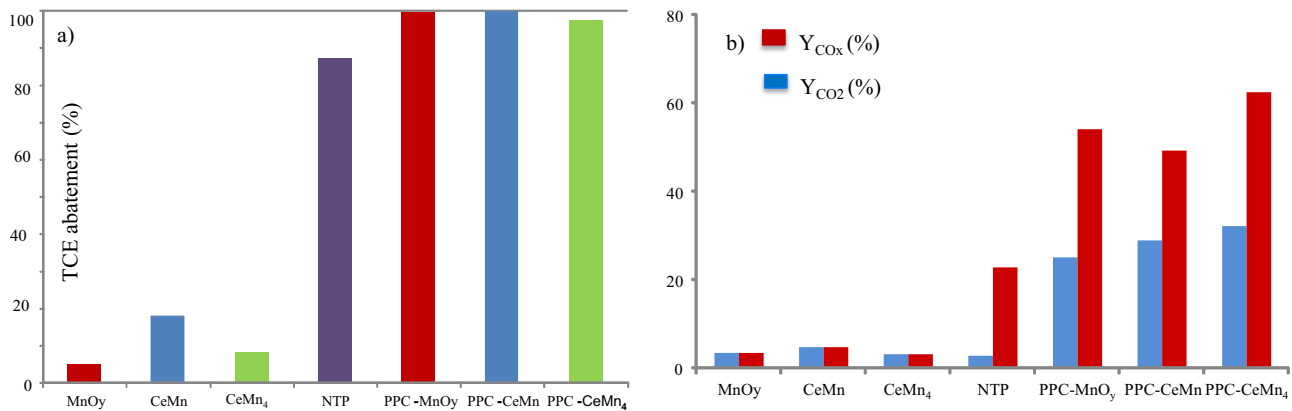


Fig. 7. a) η_{TCE} conversion and b) CO_x and CO₂ yields with catalysts alone (150 °C), in NTP alone (RT, 240 J/L) and in PPC experiments (240 J/L).

dichloroacetylchloride (DCAC) and trichloroacetaldehyde (TCAD) as incomplete gaseous oxidation products in accordance with a previous study [26]. TCE is also decomposed to a lesser extent to CO₂, CO and HCl. Formation of O₃ is also detected in the outlet stream which amounts 350 to ppm at 240 J/L. A small amount of N₂O is also detected due to N₂ oxidation. Regarding the assisted catalysts, total TCE removal is observed in the presence of MnO_y and CeMn catalysts while a very small contribution of TCE still remains in the presence of CeMn₄ oxide. The IR absorption bands characteristic of DCAC and TCAD strongly decrease for CeMn and MnO_y and are absent for the CeMn₄ sample. The IR bands relative to PG positioned at about 1820 and 1832 cm⁻¹ decrease in intensity in accordance with the sequence CeMn > MnO_y > CeMn₄. These results indicate the better ability of CeMn₄ to transform almost all of the toxic gaseous by-products generated by the plasma. However, two new bands at 794 and 773 cm⁻¹ have been detected in all PPC experiments. These bands have been ascribed to the νC–Cl vibrations of CCl₄ and HCCl₃, respectively. These new C1 chlorinated species may be likely formed through recombination of adsorbed species resulting from carbon–carbon bond cleavage of DCAC and TCAD. Furthermore, the absence of O₃ shows that all samples are active

ozone-decomposition catalysts. Formation of NO₂, not detected by the NTP, is also observed.

3.4. XPS studies of the used catalysts

Table 1 shows the atomic XPS composition after PPC. Cl has been detected in all samples. In order to quantify the Cl amount in interaction with the metal, the XPS atomic Cl/(Ce + Mn) ratio is used which allows to rank the catalysts by increasing Cl amount: MnO_y (0.09) < CeMn₄ (0.15) < CeMn (0.23). Hence, Cl deposit amount increases with Ce content in the sample. However, it has been noticed that potassium still remains on the CeMn₄ sample despite several washing steps with water. The Cl 2p spectra of the tested catalysts are illustrated in Fig. 10. The decomposition of the Cl 2p XPS signal shows two distinct Cl components for MnO_y and CeMn samples, each one composed of 2 peaks: Cl 2 p_{3/2} and Cl 2 p_{1/2} due to the spin-orbit interaction, and one component for CeMn₄. The peak observed at 200.9 ± 0.2 eV has been ascribed to organic Cl while the peak at lower B.E. (198.6–198.8 eV) is associated with mineral Cl which is the predominant phase. However, analysis of the data precludes from elucidating the preferential metallic site

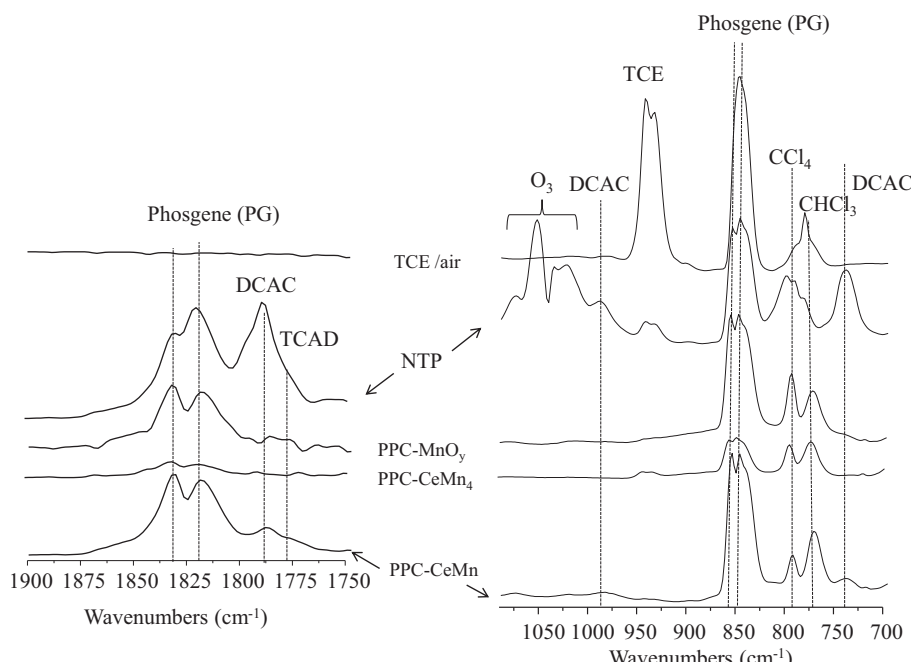


Fig. 8. FT-IR spectra of the gaseous phase at the exit of the catalytic reactor between 700–1100 and 1750–1900 cm⁻¹.

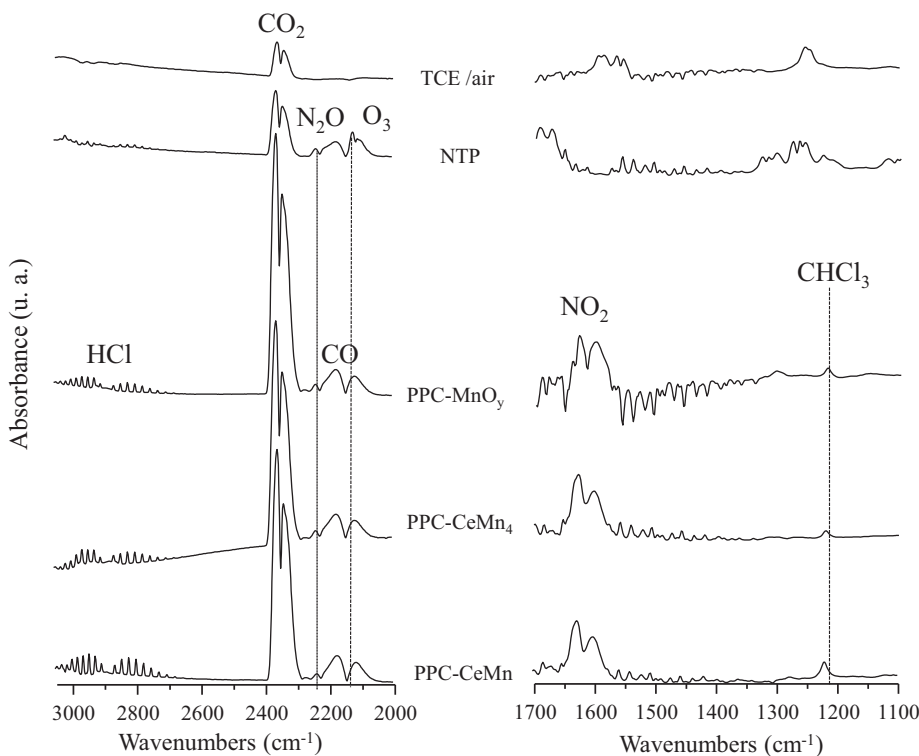


Fig. 9. FT-IR spectra of the gaseous phase at the exit of the catalytic reactor between 2000–3050 and 1100–1700 cm⁻¹.

Table 1
XPS characterizations of fresh and used catalysts.

Catalysts	XPS composition Fresh	Used	Cl/(Ce + Mn) %	Cl _{min} /(Ce + Mn) %	Cl _{org} /(Ce + Mn) %	Cl _{min} %	Cl _{org} %	BE(Cl 2 p _{3/2}) _{min} /eV	BE(Cl 2 p _{1/2}) _{org} /eV
CeMn	CeMn _{1.04} O _{3.4} C _{1.42} Cl _{0.04}	CeMn _{0.92} O _{3.35} C _{1.37} Cl _{0.44}	23	15.4	7.6	67	33	198.8	201.1
CeMn ₄	CeMn _{4.27} O _{8.96} C _{0.33} K _{0.8} Cl _{0.14}	CeMn _{3.74} O _{7.66} C _{0.52} K _{0.5} Cl _{0.71}	15	15	0	100	0	198.6	–
MnO _y	MnO _{1.43} C _{0.66} Cl _{0.015}	MnO _{1.33} C _{0.58} Cl _{0.09}	9	7.4	1.6	82	18	198.7	200.8

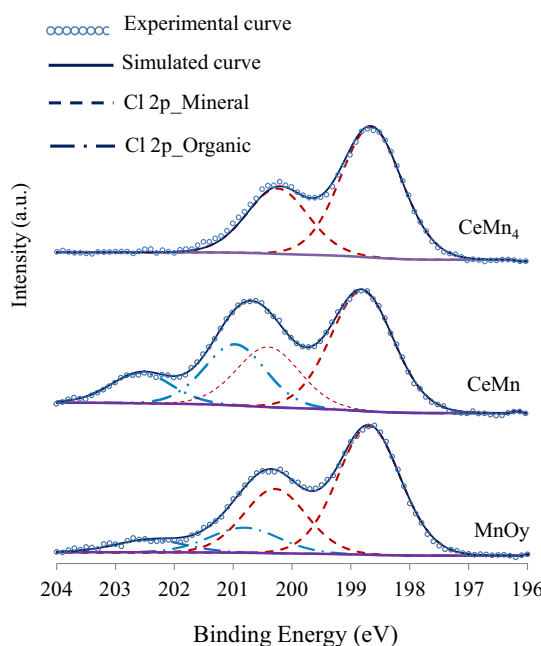


Fig. 10. XPS decomposition of the Cl 2p envelope.

prone to chlorination to give either metallic oxichlorides or/and chlorides. Regarding the organic Cl component, adsorbed species like C_xCl₂ (200.7 eV [38]) and C_xCl₃ (200.8 eV [38]) may account for the found experimental BE values. These strong organic residues can induce catalyst poisoning thereby decreasing the performance of the NTP assisted catalysts. Furthermore, XPS analysis reveals the presence of a K 2p component constituted of K 2p_{1/2} and K 2p_{3/2} peaks positioned at 292.8 and 295.6 eV for the CeMn₄ sample which shift to approximately 0.4 eV at higher BE after test. The presence of K can lead to the formation of a K-birnessite structure at the surface of the catalyst. Failure to observe the Cl organic phase over CeMn₄ could be due to the presence of K⁺ allowing a modification of the nature of the active sites facilitating the destruction of phosgene.

3.5. Scheme of TCE degradation

A simplified degradation scheme of TCE by plasma-catalysis is proposed based on the identified intermediates and by-products. Firstly, electron-molecule collisions convert N₂ and O₂ into a mixture of excited and radical species that are able to decompose TCE. The homogeneous reactions in the discharge zone give rise to mineralization products of TCE, such as CO_x, HCl and Cl₂. Molecular oxygen is also involved in a three body reaction leading to the formation of O₃. Furthermore, some unwanted polychlorinated by-products, such as dichloroacetylchloride, phosgene and

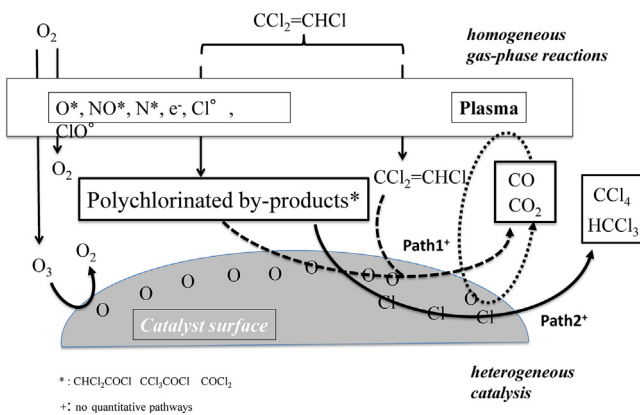


Fig. 11. Scheme of TCE degradation in PPC experiment.

trichloroacetaldehyde have been detected. The residual TCE, polychlorinated by-products and sub-products of TCE degradation can then diffuse to the catalyst surface. At that stage, the polychlorinated organic by-products can be mainly oxidized into CO_2 over the catalysts by means of active oxygen species owing to path 1 (Fig. 11). The catalysts take advantage of their high efficiency to decompose plasma generated ozone into active oxygen species. On the other hand, the formation of HCCl_3 and CCl_4 may be explained by the decomposition of DCAC and TCAD through C–C bond cleavage accompanied with subsequent Cl transfer owing to path 2 (Fig. 11). A better tolerance to Cl species, probably linked to the presence of potassium, seems to favor path 1 respective to path 2 for CeMn_4 .

4. Conclusion

In this work, the abatement of TCE was investigated in moist air ($\text{RH} = 10\%$; $\text{CO}_2: 520 \text{ ppmv}$; 150°C) with NTP using a 5-pin-to-plate negative DC corona discharge and with PPC using well dispersed nanosized CeMn_xO_y oxides as catalysts which are compared with a MnO_y oxide sample used as a reference. The well dispersed CeMn_x catalysts, synthesized by a modified “redox- precipitation” route, show outstanding physico-chemical properties in terms of textural properties (high surface exposure). PPC was found to be the best process to convert TCE into CO_2 compared to total catalytic oxidation and NTP processes due to the ability of the catalysts to completely decompose NTP generated ozone. In terms of CO_2 yieldsthe best plasma-assisted performance observed for CeMn_4 could be interpreted by a better tolerance to poisoning from Cl organic species.

Acknowledgements

The authors would like to thank the Nord Pas de Calais region – CNRS for a PhD fellowship. The authors would like to thank the PHC Tournesol FL (n°25462PJ) and IRENI for financial support. The authors thank Arnaud Beaureain for performing the XPS study.

References

- [1] J. Van Durme, J. Dewulf, C. Leys, H. Van Langenhove, *Appl. Catal. B Environ.* 78 (3–4) (2008) 324.
- [2] H.L. Chen, H.M. Lee, S.H. Chen, M.B. Chang, S.J. Yu, S.N. Li, *Environ. Sci. Technol.* 43 (2009) 2216.
- [3] A.M. Vandenbroucke, R. Morent, N. De Geyter, C. Leys, *J. Hazard. Mater.* 195 (2011) 30–54.
- [4] A.M. Vandenbroucke, R. Morent, C. De Geyter, C. Leys, *J. Adv. Oxid. Technol.* 14 (2011) 165.
- [5] A.M. Vandenbroucke, R. Morent, N. De Geyter, C. Leys, *J. Adv. Oxid. Technol.* 15 (2012) 232.
- [6] T. Oda, T. Takahashi, S. Kohzuma, *IEEE Trans. Ind. Appl.* 37 (4) (2001) 965.
- [7] T. Oda, T. Takahashi, K. Yamaji, *IEEE Trans. Ind. Appl.* 38 (3) (2002) 873.
- [8] T. Oda, T. Takahashi, K. Yamaji, *IEEE Trans. Ind. Appl.* 35 (2) (2002) 373.
- [9] T. Oda, K. Yamaji, T. Takahashi, *IEEE Trans. Ind. Appl.* 40 (2) (2004) 430.
- [10] R. Morent, J. Dewulf, N. Steenhaut, C. Leys, H. Van Langenhove, *J. Adv. Oxid. Technol.* 9 (1) (2006) 53.
- [11] M. Magureanu, N.B. Mandache, V.I. Parvulescu, C. Subrahmanyam, A. Renken, L. Kiwi-Minsker, *Appl. Catal. B: Environ.* 74 (3–4) (2007) 270.
- [12] C. Subrahmanyam, A. Renken, L. Kiwi-Minsker, *Chem. Eng. J.* 134 (1–3) (2007) 78.
- [13] T. Oda, K. Yamaji, T. Takahashi, *IEEE Trans. Conf. Rec. 2002 IEEE Ind. Appl. Conf.* 1–4 (2002) 1822.
- [14] S.B. Han, T. Oda, R. Ono, *IEEE Trans. Ind. Appl.* 41 (5) (2005) 1343.
- [15] S.B. Han, T. Oda, *Plasma Sources Sci. Technol.* 16 (2) (2007) 413.
- [16] M. Magureanu, N.B. Mandache, J.C. Hu, R. Richards, M. Florea, V.I. Parvulescu, *Appl. Catal. B: Environ.* 76 (3–4) (2007) 275.
- [17] S.T. Oyama, *Chemical and catalytic properties of ozone*, *Catal. Rev. Sci. Eng.* 42 (2007) 279.
- [18] B. Dhandapani, S.T. Oyama, *Gas phase ozone decomposition catalysts*, *Appl. Catal. B: Environ.* 11 (1997) 129.
- [19] F. Arena, G. Trunfio, J. Negro, B. Fazio, L. Spadaro, *Chem. Mater.* 19 (2007) 2269–2276.
- [20] F. Arena, G. Trunfio, J. Negro, B. Fazio, L. Spadaro, *Ind. Eng. Chem. Res.* 46 (2007) 6724–6731.
- [21] F. Arena, G. Trunfio, B. Fazio, L. Spadaro, *J. Phys. Chem. C* 113 (2009) 2822–2829.
- [22] M.T. Nguyen Dinh, J.-M. Giraudon, J.-F. Lamonier, A. Vandenbroucke, N. De Geyter, C. Leys, R. Morent, *Appl. Catal. B: Environ.* 147 (5) (2014) 904–911.
- [23] Y.S. Akishev, A.A. Deryugin, I.V. Kochetov, A.P. Napartovich, N.I. Trushkin, *J. Phys. D: Appl. Phys.* 26 (1993) 1630.
- [24] Y.S. Akishev, M. Grushin, I.V. Kochetov, A.P. Napartovich, M. Pan'kin, N.I. Trushkin, *Plasma Phys. Rep.* 26 (2000) 157.
- [25] Y.S. Akishev, O. Goossens, T. Callebaut, C. Leys, A.P. Napartovich, N.I. Trushkin, *J. Phys. D: Appl. Phys.* 34 (2001) 2875.
- [26] A.M. Vandenbroucke, R. Aerts, W. Van Gaens, N. De Geyter, C. Leys, R. Morent, A. Bogaerts, *Plasma Chem. Plasma Process.* 35 (2015) 217.
- [27] R. Morent, C. Leys, *Ozone Sci. Eng.* 27 (2005) 239.
- [28] R. Craciun, *Catal. Lett.* 55 (1998) 25.
- [29] X. Zheng, S. Wang, X. Wang, S. Wang, X. Wang, S. Wu, *Mater. Lett.* 59 (2005) 2769.
- [30] S. Tsunekawa, R. Sivamohan, S. Ito, A. Kasuya, T. Fukuda, *Nanostruct. Mater.* 11 (1999) 141.
- [31] V.R. Galakhov, M. Demeter, S. Bartkowiak, M. Neumann, N.A. Ovechkina, E.Z. Kurmaev, N.I. Logachevskaya, Y.M. Mukovskii, J. Mitchell, D.L. Ederer, *Phys. Rev. B* 65 (2002) 1131021–1131024.
- [32] S. Franger, S. Bach, J. Farcy, J.-P. Farcy, J.P. Peirera-Ramos, N. Baffier, *J. Power Sources* 109 (2002) 262.
- [33] J. Zhou, L. Yu, M. Sun, S. Yang, F. Ye, J. He, Z. Hao, *Ind. Eng. Chem. Res.* 52 (2013) 9586–9593.
- [34] C. Julien, M. Massot, R. Baddour-Hadjean, S. Franger, S. Bach, J.-P. Pereira-Ramos, *Solid State Ionics* 159 (2003) 345.
- [35] C. Julien, M. Massot, *Phys. Chem. Chem. Phys.* 4 (2002) 4226–4235.
- [36] Y. Luo, Y.-Q. Deng, W. Mao, X.-J. Yang, K. Xu, Y.-F. Han, *J. Phys. Chem. C* 116 (2012) 20975–20981.
- [37] C.B. Azzoni, M.C. Mozzati, P. Galinetto, A. Paleari, V. Massarotti, D. Capsoni, M. Bini, *Solid State Commun.* 112 (1999) 375–378.
- [38] C.D. Wagner, W.M. Riggs, L.E. Davis, J.F. Mulder, *Handbook of X-ray Photoelectron Spectroscopy*, in: G.E. Muilenberg (Ed.), PerkinElmer Corporation, Eden Prairie, 1978.